Available online at www.sciencedirect.com
SCIENCE DIRECT®
Journal of Solid State Chemistry 178 (2005) 3485–3493
JOURNAL OF SOLID STATE CHEMISTRY
www.elsevier.com/locate/jssc

A magnetic organic–inorganic composite: Synthesis and characterization of magnetic 5-aminosalicylic acid intercalated layered double hydroxides

Hui Zhang*, Kang Zou, Hui Sun, Xue Duan*

Ministry of Education Key Laboratory of Science and Technology of Controllable Chemical Reactions, Box 98, Beijing University of Chemical Technology, Beijing 100029, China

Received 13 June 2005; received in revised form 26 August 2005; accepted 6 September 2005
Available online 10 October 2005

Abstract

A core–shell structured magnetic layered organic–inorganic material involving 5-aminosalicylic acid (5-ASA) intercalated Zn–Al layered double hydroxides (LDHs) and magnesium ferrite ($MgFe_2O_4$) is assembled by a coprecipitation method. The powder X-ray diffraction results show the coexistence of the clear but weak diffractions of $MgFe_2O_4$ and ordered relatively stronger reflections of 5-ASA intercalated LDHs. The TEM image of magnetic 5-ASA intercalated LDHs reveals that the LDHs layer covers the $MgFe_2O_4$ particles or their aggregates with particle size of 50–80 nm. The vibration sample magnetization (VSM) measurements exhibit the increase in saturation magnetization of magnetic 5-ASA intercalated LDHs samples with increasing amount of magnetic core. The XPS analyses account for a majority of Zn, Al and O atoms on the surface of magnetic particles. It is suggested that the magnetic core $MgFe_2O_4$ was coated with LDHs layer probably through Zn–O–Mg and Al–O–Mg linkages, and a core–shell structured model is tentatively proposed.

Keywords: Layered double hydroxides; Magnetic materials; Coprecipitation; X-ray diffraction; 5-asa intercalation; Magnetic properties

1. Introduction

Layered double hydroxides (LDHs), also named as anionic clays or hydrotalcite-like compounds, represented by the general formula $[M^{2+}_{1-x}M^{3+}_x\ (OH)_2]\cdot A_{x/n}\cdot yH_2O$, where M^{2+} and M^{3+} are metal cations, $x = M^{3+}/(M^{2+}+M^{3+})$ and A^{n-} denotes the interlayer anions. In these compounds the hydroxide layers are built up by metal cations occupying the centers of octahedral group shared by three octahedral cations and pointing to the interlayer region [1]. The magnesium aluminum hydrotalcite behaves biocompatible [2] and has found pharmaceutical applications as an antacid [3,4]. Evidently, LDHs have a remarkable property that a variety of anionic species can be inserted as guests into the interlamella of the LDHs, especially beneficial organic anions. In this role they have been used extensively as ion-exchange materials, catalysts, sorbents and halogen absorbers [2]. More recently, there have been a tremendous number of new developments using these materials to store and deliver biologically active agents. O'Hare's group [5,6] and Ambrogi et al. [7,8] have been focusing on the drug–inorganic hybrid materials, and a series of pharmaceutically active species including diclofenac, gemfibrozil, ibuprofen, naproxen, 2-propylpentanoic acid, 4-biphenylacetic acid and tolfenamic acid can be reversibly intercalated into layered double hydroxide with different layer metallic compositions by anion exchange method, and their initial in vitro studies suggest that these materials may have potential applications as the basis of a novel tunable drug delivery system.

5-aminosalicylic acid (commercial name as Mesalazine) is widely used in the treatment of inflammatory bowel disease, including ulcerative colitis and Crohn's disease [9]; however when orally administered, 5-aminosalicylic acid is unstable in the gastric conditions and prone to be absorbed in the upper intestine, which causes low drug bioavail-

*Corresponding authors. Fax: +8610 64425385.
E-mail addresses: huizhang67@gst21.com (H. Zhang), duanx@mail.buct.edu.cn (X. Duan).

0022-4596/$ - see front matter © 2005 Elsevier Inc. All rights reserved.
doi:10.1016/j.jssc.2005.09.008

ability and low efficiency for inflammatory colon disease. In the past decades, the primary approaches to obtain colon-specific drug delivery showed limited success including prodrugs [10], pH-dependent systems [11], and microflora-actived systems [12]. Hence, continuous efforts have been focused on designing colon-specific delivery systems with improved site specificity and versatile drug release kinetics to accommodate different therapeutic needs. Magnetic drug delivery has been an active field of study for at least two decades [13]. In the 1970s, Widder et al. [14] proposed the concept of magnetic targeting to inject a magnetically susceptible material coated with a drug-laden matrix and then to use an externally placed magnet to guide the drug matrix to the targeted site. Targeting drug is affected with a magnet of sufficient strength and focuses on retaining the particles in a flow field, such as that found in the vasculature feeding a tumor. An optimum particle would extravagate into the tissue and be physically retained. In the early 1980s, Widder et al. [15] firstly used external magnets to target drugs, which had been bound to activated carbon mixed with iron. However, the approach became feasible only when ferrous oxide magnets, which have a greater depth of penetration, replaced elemental iron magnet. The magnetic drug targeting is commonly a core–shell structured composite [16], which constructed by binding drug-biocompatible complexes to the surface of magnets nanoparticles or their aggregates. The first article employed colloidal magnetite (Fe_3O_4) coated with cross-linked albumin, and the resultant microspheres were used to encapsulate doxorubicin, and were captured magnetically in Yoshida sarcoma tumors implanted in rat tails [17].

Usually both ferromagnetism substances and ferrimagnetism substances are generally called magnetism substance. In detail, Fe_3O_4 is a strong magnetic material because of belonging to ferromagnetism substances, while magnesium ferrite is a part of ferrimagnetism substance; thus it is a kind of soft magnetic materials that possess strong magnetism and high Curie temperature [18]. Ferrites have widely been applied in a good many of realm, such as bio-separation [19], enzyme [20] and protein immobilization [21]. However, ferrites are commonly produced by a ceramic process involving high temperature solid state reactions [22], sol–gel method [23], precipitation method [24], etc., and as-synthesized ferrites have some disadvantages, for instance asymmetric granule, superparamagnetic properties and weak saturation magnetization, and so forth. The ferrite with above features is not suitable to be applied in the magnetic drug targeting system [14]. Fortunately, a stoichiometric synthesis route of a pure ferrite from a tailored layered double hydroxide precursor has been developed in our Lab overcoming some shortage of conventional method [25]. And recently, Zhang et al. [26] reported a novel nanoscale magnetic solid base catalyst involving a layered double hydroxide supported on a ferrite core.

In the present paper, we report in detail an effective combination of organic–inorganic hybrid and magnetic material, i.e. a core–shell type magnetic 5-aminosalicylic acid intercalated layered double hydroxides is assembled by coprecipitation method and characterized systematically by X-ray diffraction (XRD), FT-IR, TEM, vibration sample magnetization (VSM), TG-DTA and X-ray photoelectron spectroscopy (XPS) techniques to provide useful information for potential drug targeting treatment.

2. Experimental

2.1. Materials

5-aminosalicylic acid (abbreviated as 5-ASA, purity > 95%, from Beijing Comens Chemical Co. LTD.) was used as available. All other reagents are of analytical grade.

2.2. Syntheses

2.2.1. Magnetic material

The magnetic nanoparticles were prepared following the method described previously [26,27]. A mixed aqueous solution of $Mg(NO_3)_2 \cdot 6H_2O$ (0.033 mol) and $Fe(NO_3)_3 \cdot 9H_2O$ (0.067 mol) in deionized water and a second solution containing NaOH ($[NaOH] = 1.6\ [Mg^{2+} + Fe^{3+}]$) and Na_2CO_3 ($[CO_3^{2-}] = 2.0[Fe^{3+}]$) in deionized water (pH~9) were simultaneously added to a colloid mill [28,29] rotating at 4000 rpm and mixed for 2 min. The resulting slurry was removed from the reactor into a three-neck flask and aged at 373 K for 6 h. The final precipitate was filtered, washed thoroughly with deionized water and dried at 343 K for 24 h. The resulting sample MgFe-LDHs was then calcined at 1173 K for 2 h giving the magnetic material, denoted as $MgFe_2O_4$.

2.2.2. 5-ASA intercalated LDHs

5-ASA intercalated LDHs were synthesized by coprecipitation method. A mixed aqueous solution of $Zn(NO_3)_2 \cdot 6H_2O$ and $Al(NO_3)_3 \cdot 9H_2O$ ($Zn^{2+}/Al^{3+} = 4$, $[Zn^{2+}] = 0.06$ M) in 200 ml decarbonated deionized water was kept at pH~8.4 by dropwise addition of NaOH solution (0.38 M) containing 5-ASA (0.008 mol) with vigorous stirring under N_2 atmosphere. The resulting slurry was aged at 333 K for 48 h, centrifuged, washed and dried for 12 h at 343 K, denoted as ASA-LDHs.

2.2.3. Magnetic 5-ASA intercalated LDHs

An aqueous solution of $Zn(NO_3)_2 \cdot 6H_2O$ and $Al(NO_3)_3 \cdot 9H_2O$ ($Zn^{2+}/Al^{3+} = 4$, $[Zn^{2+}] = 0.06$ M) in 200 ml decarbonated deionized water was firstly mixed with $MgFe_2O_4$ with different $Zn(NO_3)_2 \cdot 6H_2O/MgFe_2O_4$ weight ratios of 24, 18, and 5 giving a suspension. This suspension was kept at pH~8.4 by dropwise addition of NaOH solution (0.38 M) containing 5-ASA (0.008 mol) with vigorous stirring under N_2 atmosphere. The following procedures are the same as those described in Section 2.2.2. The products were denoted

as ASA-LDHs/$MgFe_2O_4$-24, ASA-LDHs/$MgFe_2O_4$-18 and ASA-LDHs/$MgFe_2O_4$-5, respectively.

For comparison, CO_3-containing LDHs were also synthesized as follows: $Zn(NO_3)_2 \cdot 6H_2O$ (0.012 mol) and $Al(NO_3)_3 \cdot 9H_2O$ (0.003 mol) were dissolved in 100 ml deionized water to make a mixed salt solution, NaOH (0.038 mol) and Na_2CO_3 (0.006 mol) were dissolved in 100 ml deionized water to make a mixed alkali solution, then the two solutions were simultaneously added to a colloid mill rotating at 4000 rpm and mixed for 2 min. The following procedures are the same as those described in Section 2.2.1. The products were denoted as CO_3-LDHs.

2.3. Characterization

Powder XRD data were taken on a Shimadzu XRD-6000 diffractometer using Cu$K\alpha$ radiation ($\lambda = 1.5418$ Å, 40 kV, 30 mA). The samples, as unoriented powders, were step-scanned in steps of 0.02°(2θ) in the range 3–70° using a count time of 4 s per step. The FT-IR spectra were obtained using a Bruker Vector-22 FT-IR spectrophotometer. KBr pellet containing 1% sample was used to obtain the FT-IR spectra. The TEM micrographs were recorded on a HITACHI-800 transmission electron microscope. Surface chemical compositions were studied by XPS using a VG ESCALAB-MKII X-ray photoelectron spectrometer. The pressure in the analysis chamber during the experiments was 2×10^{-7} Pa. Spectra were acquired using a standard Al$K\alpha$ source at $hv = 1486.6$ eV operating at 15 kV and 20 mA. The binding energy scale was reference to the C1s line of aliphatic carbon contamination set at 284.6 eV. The actual metal incorporation contents were measured by inductively coupled plasma (ICP) emission spectroscopy using a Shimadzu ICPS-7500 instrument. Thermogravimetric analyses (TG) were performed on a locally made PCT-IA at a heating rate of 10 °C/min in airflow. 5-ASA content was determined with an UV absorption spectrophotometer Shimadzu UV-2501PC at $\lambda_{max} = 309$ nm after dissolution of the samples in HCl:HNO_3 = 3:1 (mol/mol) solution. C, H, and N elemental microanalyses were obtained on an Elementar Vario Elemental Analyzer. Magnetic properties of the samples were studied on a JSM-13 Vibrating Sample Magnetometer with a magnetic field of 12 kOe.

3. Results and discussion

3.1. Crystal structure and magnetic property of $MgFe_2O_4$

The X-ray diffraction patterns of $MgFe_2O_4$ and its layered precursor are shown in Fig. 1. The XRD pattern of the precursor Mg–Fe LDHs has the characteristic diffractions as (003), (006), (009) and (110) planes of hydrotalcite-like compounds [2]. The unit cell parameter a is the average distance between two metal ions in the layers and c is three times the distance from the center of one layer to the next. The value of a ($= 2d_{110}$) is a function of the average radii

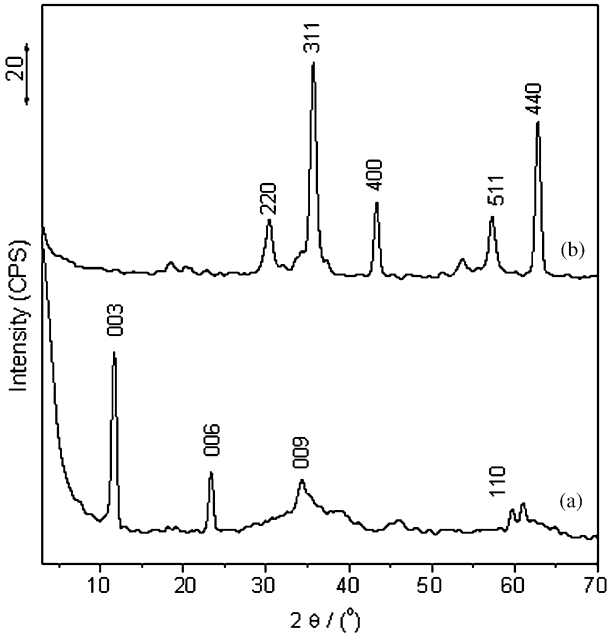

Fig. 1. XRD patterns for Mg–Fe LDHs (a) and its calcined product at 1173 K (b).

of the metal cations whilst the value of c ($= 3d_{003}$) is a function of the average charge of the metal cations, the nature of the interlayer anion and the water content. The parameter a value of 0.304 nm and c of 2.28 nm are close to the value previously reported [26]. After calcination at 1173 K, the layered structure of LDHs are completely disappeared, instead of well-shaped diffraction peaks of (220), (311), (400), (511) and (440) planes due to the formation of magnesium ferrite, which are in good agreement with the spinel structured $MgFe_2O_4$ (JCPDS 17-0465). It should be mentioned that the characteristic reflections (102) and (111) of MgO at 43.2° and 62.7° may overlap with the spinel (400) and (440) planes, but from the relative intensity of the peaks, it is possible to deduce that the amount of MgO is very small in the calcined sample. The ICP analysis shows the Mg/Fe ratio of 1:1.9, which is approximate to the initial Mg/Fe ratio within the experimental error, and near to the stoichiometric ratio in $MgFe_2O_4$. The average crystallite diameter can be estimated from the full-width at half-maximum (FWHM) of the (311) reflection by using the Scherrer equation [2]: $D = 0.89\lambda/(\beta \cos \theta)$, where λ is the X-ray wavelength, θ the Bragg diffraction angle, and β is the full-width at half-maximum. The estimated D_{311} value is 18.7 nm. The magnetic property is measured by VSM with hysteresis loop shown in Fig. 2. The specific saturation magnetization σ_s of 23.34 emu/g and coercive force of zero demonstrate that as-synthesized $MgFe_2O_4$ sample possesses strong soft magnetic properties [30], accordingly suitable to be used as magnetic substrate for further assembly investigation.

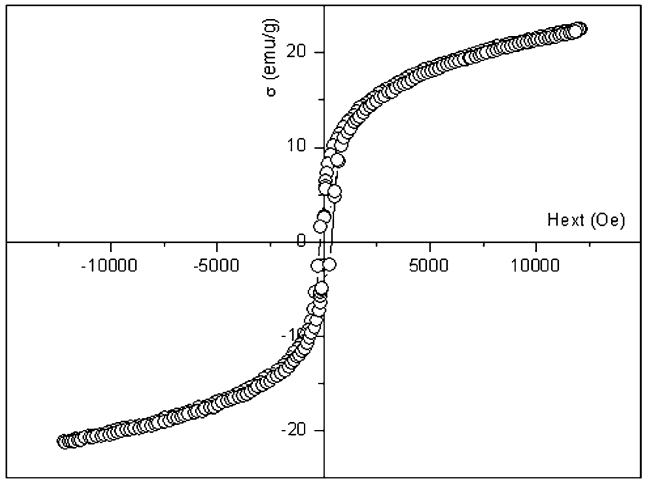

Fig. 2. Magnetization curve obtained by VSM at room temperature of $MgFe_2O_4$.

3.2. Crystal structure of magnetic 5-ASA intercalated LDHs

The XRD patterns of three magnetic 5-ASA intercalated LDHs samples together with ASA-LDHs and CO_3-LDHs are depicted in Fig. 3. It can be seen that all samples present the characteristic reflections of LDH compounds, and the basal (003) reflections shift to lower 2θ angles in the range 5–7° as compared with that of CO_3-LDHs ($2\theta = 11.78°$), indicating the intercalation of 5-ASA between the LDH layers [31]. For ASA-LDHs, d_{003} of 1.580 nm and d_{006} of 0.798 nm accord to the good multiple relationship between the basal and second-order reflections as $d_{003} = 2d_{006}$ of LDH compounds. However, for magnetic 5-ASA intercalated LDHs samples, the $d_{003} = 2d_{006}$ relationship is not strictly followed (Table 1). Clearly, with increasing amount of $MgFe_2O_4$, the intensities of the diffractions ascribed to ASA-LDHs decrease and those attributed to $MgFe_2O_4$ increase, especially for ASA-LDHs/$MgFe_2O_4$-5, which shows very weak (003) and (006) reflections due to the presence of the largest amount of $MgFe_2O_4$, which probably lead to its poor crystallinity. While for ASA-LDHs/$MgFe_2O_4$ -24 and ASA-LDHs/$MgFe_2O_4$-18, the better crystallized ASA-LDHs is observed in addition to the $MgFe_2O_4$ phase, but their d_{003} slightly reduce to 1.350–1.448 nm accompanied with a weak left shoulder with similar d_{003} to that of single ASA-LDHs, implying that the introduction of $MgFe_2O_4$ may affect the crystal structural order of ASA-LDHs phase and certain function between ASA-LDHs and $MgFe_2O_4$ may occur.

Given the thickness of 0.48 nm for Zn–Al layer [2], the interlayer spacing of ASA-LDHs estimated as 1.10 nm from its d_{003} is larger than the molecular size of 5-ASA (0.67 nm determined by the software ChemSketch), suggesting a vertically interdigitated bilayer orientation of 5-ASA between the layers, that is, with the carboxylate

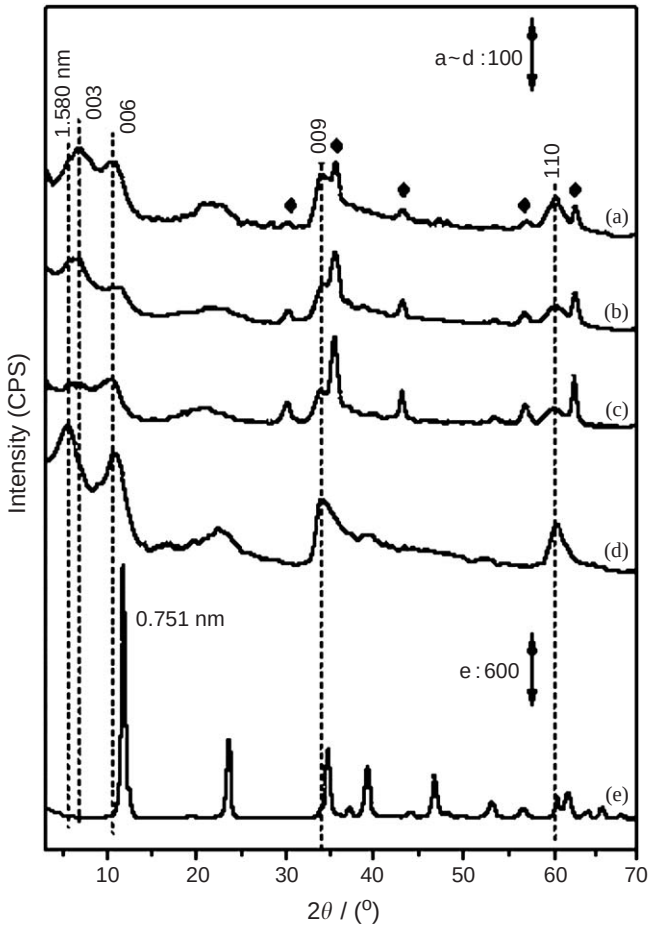

Fig. 3. XRD patterns of magnetic 5-ASA intercalated LDHs samples with different $Zn(NO_3)_2.6H_2O/MgFe_2O_4$ weight ratios. (a) 24, (b) 18 and (c) 5, and (d) ASA-LDHs and (e) CO_3-LDHs. (♦$MgFe_2O_4$).

anions pointing alternatively to both hydroxide layers. In the case of magnetic 5-ASA intercalated LDHs, the interlayer spacing calculated as 0.89–0.97 nm is still larger than the molecular size of 5-ASA, implying that the vertically interdigitated bilayer in ASA-LDHs may be interfered due to the interaction between the magnetic $MgFe_2O_4$ phase and ASA-LDHs layer, and consequently resulting in a tilted close-packed bilayer orientation of 5-ASA in magnetic 5-ASA intercalated LDHs samples.

The Zn/Al ratios based upon ICP analyses, lattice parameters a and c derived from XRD patterns, and related data for magnetic 5-ASA intercalated LDHs samples are summarized in Table 1. It can be seen that the Zn/Al ratios of products are quite different from the initial Zn/Al ratio (4/1) in the mother liquor. The higher Zn/Al ratio of 3.30 for ASA-LDHs/$MgFe_2O_4$-24 results in its smaller layer charge density ($x = 0.230$) and consequently larger parameter a of 0.306 nm than other two samples (Table 1), and this is reasonably owing to the larger ionic radius of Zn^{2+} (0.074 nm) than Al^{3+} (0.050 nm) [2]. Also this a value is exactly the same as that of the single ASA-LDHs much probably due to its lowest $MgFe_2O_4$ content. The 5-ASA loadings increase with

Table 1
Analysis data of magnetic 5-ASA intercalated LDHs samples and ASA-LDHs

Samples	ASA-LDHs/$MgFe_2O_4$-24	ASA-LDHs/$MgFe_2O_4$-18	ASA-LDHs/$MgFe_2O_4$-5	ASA-LDHs
d_{003} (nm)	1.35	1.448	1.305	1.580
d_{006} (nm)	0.829	0.788	0.839	0.798
d_{110} (nm)	0.153	0.148	0.148	0.153
c (nm)[a]	4.05	4.344	3.915	4.74
a (nm)[a]	0.306	0.296	0.296	0.306
Zn/Al[b]	3.30	2.90	2.80	2.90
x[c]	0.230	0.256	0.260	0.256
5-ASA (%)	17.0	17.6	17.9	19.8
σ_s (emu/g)	1.53	2.90	4.61	—

[a]Hydrotalcites crystallize is in hexagonal symmetry, and the unit cell parameters being c and a can be calculated according to $c = 3c' = 3d_{003}$, $a = 2d_{110}$ [26].
[b]Determined by ICP analysis.
[c]x = Al/(Zn + Al) denoting the layer charge density of LDHs.

decreasing Zn/Al ratios as shown in Table 1, and this quite accords to the charge balance principle of LDHs compound [2,32]. However, the lattice parameter c of three magnetic 5-ASA intercalated LDHs samples do not give the regular monotone change with decreasing Zn/Al ratios, but they are greatly decreased compared to that of the single ASA-LDHs. This can be explained by the interaction between the magnetic $MgFe_2O_4$ phase and layered ASA-LDHs phase, which probably influence the interlayer arrangement of 5-ASA anions and result in the less regular changes of lattice parameter c values. In addition, the characteristic diffractions of $MgFe_2O_4$ phase can be clearly observed in Fig. 3 at 2θ angles of 30.36°, 35.68°, 43.33°, 57.23° and 62.82° with lower intensities due to their relative lower content, and obviously these peak intensities in magnetic 5-ASA intercalated LDHs samples increase with increasing amount of $MgFe_2O_4$ involved. This suggests that the relative independence of $MgFe_2O_4$ phase and ASA-LDHs phase is maintained in this new kind of magnetic organic–inorganic hybrid.

Fig. 4 shows the FT-IR spectra of 5-ASA, ASA-LDHs, ASA-LDHs/$MgFe_2O_4$-24 and $MgFe_2O_4$. The characteristic absorptions of 5-ASA presented in Fig. 4a can be attributed as follows: (1) 1647 cm^{-1} to C=O stretching vibration, and (2) 1575 cm^{-1} and 1450 cm^{-1} to -NH bending vibration and C–N stretching vibration, respectively [33]. For ASA-LDHs and ASA-LDHs/$MgFe_2O_4$-24 (Fig. 4b and c) the broad absorption band between 3400 and 3600 cm^{-1} arises from the stretching vibrations of –OH group in the brucite-like layer and physisorbed water. Taking into consideration the reaction pH (~8.4) and the acid–base properties of 5-ASA described by three equilibria with $pK_{a1} = 2$, $pK_{a2} = 5.8$, and $pK_{a3} = 12$ [34], the distribution coefficient values can be calculated as $\delta_0 = 0.025\%$, $\delta_1 = 99.7\%$, $\delta_2 = 0.25\%$, and $\delta_3 = 10^{-7}\%$. Thus, 5-ASA exists mainly as the monovalent anion $C_7H_6NO_3^-$ with a $-CO_2^-$ group (99.72%). Reasonably, two bands at ca. 1619 and 1378 cm^{-1} for ASA-LDHs and ASA-LDHs/$MgFe_2O_4$-24 are assigned to the anti-symmetric and symmetric stretching of $-CO_2^-$, further indicating the successful intercalation of 5-ASA [35]. Moreover, referred to the FT-IR spectra of 5-ASA, it can be concluded that for ASA-LDHs/$MgFe_2O_4$-24, the positions of the $-CO_2^-$ groups (1647 and 1385 cm^{-1}) shift to low wavenumbers (1619 and 1378 cm^{-1}) owing to hydrogen bonding between $-CO_2^-$ groups and hydroxyl groups of Zn–Al layers, whereas the position of the –NH group remains unchanged. The strong and sharp band at ca. 578 cm^{-1} attributing to M–O lattice vibration in the FT-IR spectrum of $MgFe_2O_4$ clearly reappears in FT-IR spectrum of ASA-LDHs/$MgFe_2O_4$-24, implying the potential association of magnetic material to ASA-LDHs. In spite of the N_2 protection, the presence of small amounts of carbonate in products is observed with considerable weak absorption in ASA-LDHs/$MgFe_2O_4$ (1370 cm^{-1}) and possibly overlapped by the symmetric stretching absorption of $-CO_2^-$ group.

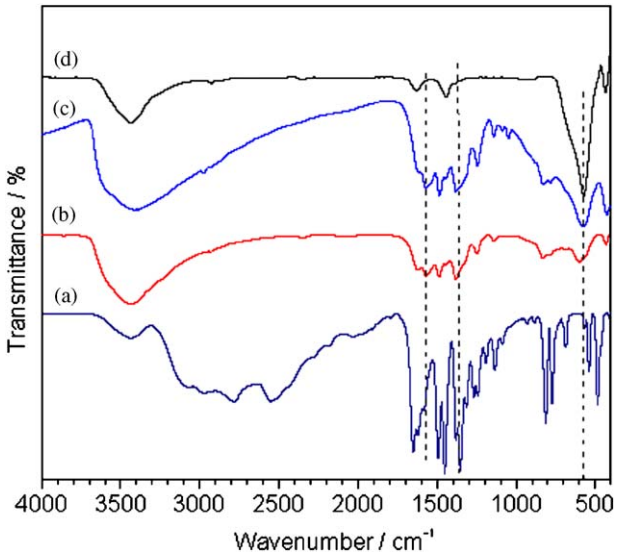

Fig. 4. FT-IR spectra of 5-ASA (a), ASA-LDHs (b), ASA-LDHs/$MgFe_2O_4$-24 (c) and $MgFe_2O_4$ (d).

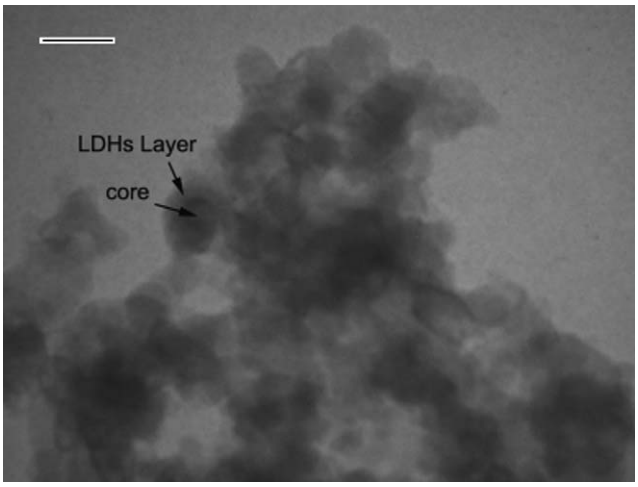

Fig. 5. The TEM photo of ASA-LDHs/$MgFe_2O_4$-24 (Scale bar = 50 nm).

3.3. Morphology and magnetic property

Fig. 5 depicts the TEM image of ASA-LDHs/$MgFe_2O_4$-24. It is clearly seen that a network-like image of nanocomposite particles or their aggregates is formed. In spite of some extent aggregation, it still can be observed that the larger size of composite with diameters of 50–80 nm has been obtained, and the core–shell structure is marked by dark colored $MgFe_2O_4$ core coated with gray ASA-LDHs shell which presents approximate hexagonal plate-like crystallites [26].

The magnetic property measurement of ASA-LDHs/$MgFe_2O_4$ composites at ambient temperature by using VSM reveal that the saturation magnetization σ_s (1.53–4.61 emu/g in Table 1) of the three samples are lower than that of the $MgFe_2O_4$ (23.34 emu/g), and also σ_s value increases with increasing amount of $MgFe_2O_4$ employed, attributed mainly to the contribution of the volume of the non-magnetic coating layer to the total sample volume. In addition, the non-magnetic coating layer can be considered as a magnetically inert layer on the surface of a magnetic material. It is noted that relatively higher saturation magnetization of ASA-LDHs/$MgFe_2O_4$-5 is obtained. This phenomenon can be attributed to a relatively higher magnetic material content of this sample, and therefore the existence of a few uncoated magnetic nanoparticles and simultaneously a few free ASA-LDHs microcrystallites is possible.

3.4. Thermal stability

The TG and DTA curves of the CO_3-LDHs, ASA-LDHs and ASA-LDHs/Mg Fe_2O_4 -24 are depicted in Fig. 6a and b. In the case of the CO_3-LDHs as a reference sample, there are two obvious mass losses observed in Fig. 6a. An extremely weak mass loss observed before 100 °C indicates that the amount of physical adsorbed water at the external surface of the crystallites is very small. A following rapid

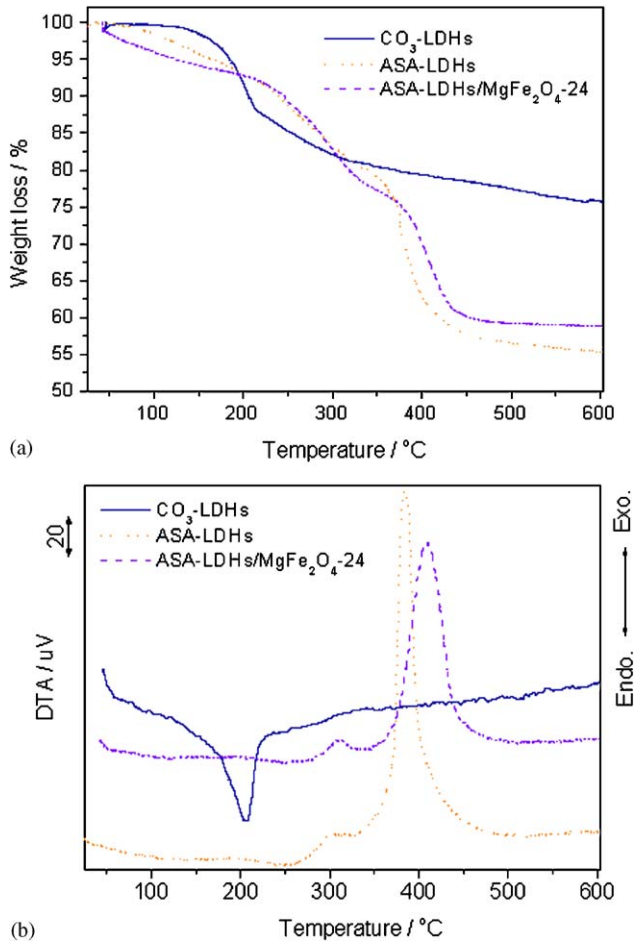

Fig. 6. The TG (a) and DTA (b) profiles of CO_3-LDHs, ASA-LDHs and ASA-LDHs/$MgFe_2O_4$-24.

mass loss in the temperature region 100–210 °C is due to the removal of the interlayer water molecules, which is quite strongly attached to the hydroxide layer and/or interlayer anion via hydrogen bonds, and the interlayer balancing anion CO_3^{2-}. And consequently a very strong DTA endothermic effect at 205 °C is observed in Fig. 6b. Then a gentle mass loss in the higher temperature range from 210 to 325 °C up to 500 °C is attributed to the dehydroxylation of the LDH basal layer [2]. However, the TG curves of ASA-LDHs and ASA-LDHs/$MgFe_2O_4$-24 clearly show a series of continuous weight losses in the region 25–330 °C and a rapid one between 330 and 500 °C. The corresponding DTA plots show a very weak endothermic peak at ca. 140 °C due to the removal of physisorbed water and a little big one at ca. 250 °C due to the removal of the interlayer structure water and a very few cointercalated CO_3^{2-} anions [2,31]. The latter endothermic peak temperature is obviously higher than that of CO_3-LDHs, demonstrating that the interlayer water in ASA-LDHs and ASA-LDHs/$MgFe_2O_4$-24 are more strongly attached to the LDH layer and/or interlayer anion via hydrogen bonding. More differently, a weak but distinguishable exothermic peak in the region 280–330 °C,

quite near to the melting and decomposition temperatures of 5-ASA at 278 and 298 °C [36], is ascribed to the combination effect resulting from the dehydroxylation of the LDHs layer, and the melt and decomposition/combustion of small amount of interlayer organic species 5-ASA anions. The last remarkably strong exothermic effect around 380–410 °C is mainly attributed to the combustion of the intercalated 5-ASA under air atmosphere [37] and trace to the continued dehydroxylation of the LDHs layer, accompanied with the formation of mixed ZnAl oxide [2,31]. From TG curve it is easily obtained that the mass loss in the region 350–500 °C of ASA-LDHs and ASA-LDHs/$MgFe_2O_4$-24 is 21.5% and 18.3%, respectively, both are close to the UV-measured 5-ASA loadings (19.8% and 17.0% in Table 1). Moreover, the 5-ASA mass percentage of 21.5% in ASA-LDHs LDH is in good agreement with an estimated chemical formula $Zn_{2.9}Al(OH)_8(ASA^-)_{0.64}(CO_3^{2-})_{0.08}\cdot H_2O$ based upon elemental analysis and TG results, where 5-ASA is about 20.6% in weight, confirming that 5-ASA species as monovalent in as-synthesized LDHs composite, in accordance with previous analysis.

Furthermore, it is noted that 5-ASA anions in both ASA-LDHs and ASA-LDHs/$MgFe_2O_4$-24 were completely decomposed above 380 °C, confirming the enhanced thermal stability of intercalated 5-ASA due to the host–guest interaction between 5-ASA anion and LDH layer as indicated by FT-IR analyses, compared to that of pure 5-ASA (292 °C). Moreover, it should also be noted that the major exothermic effect of ASA-LDHs/$MgFe_2O_4$-24 is presented at higher temperature (408 °C) than that of ASA-LDHs (384 °C), implying the further enhanced thermal stability of intercalated 5-ASA in magnetic 5-ASA intercalated LDHs hybrid composite possibly due to the interactions between the ASA-LDHs layer and $MgFe_2O_4$ phase.

3.5. Surface composition and structural model

To investigate the interactions between ASA-LDHs layer and $MgFe_2O_4$ phase and the microstructure of magnetic 5-ASA intercalated LDHs, the surface chemical compositions were measured by XPS technique. For comparison, XPS data of $MgFe_2O_4$, ASA-LDHs and ASA-LDHs/$MgFe_2O_4$-24 are altogether summarized in Table 2. In 1 nm depth profiles examined by XPS, there are no signals due to Mg and Fe detected on the surface of ASA-LDHs/$MgFe_2O_4$-24, whereas signals of Zn, Al and O are very strong with atom percentages of 31.9%, 8.73%, and 59.24%, respectively. This indicates that the Mg and Fe are more likely to be positioned in the interior rather than on the surface, suggesting a core–shell structure with $MgFe_2O_4$ as the core coated with ASA-LDHs phase.

In order to confirm this hypothesis, the different depth profiles were studied by means of argon (4 kV, 25 μA target current) sputtering/cleaning of the specimens. The sputtering rate is 1 nm/min [38]. The Fe2*p* narrow scanning XPS survey spectra at different depth profiles could reveal surface layer information as shown in the Fig. 7. After 5 min sputtering equal to a 5 nm depth profile, the Fe2*p* is not observed, indicating that Fe is not located in the surface layer. After 20 min sputtering, the Fe2*p* signal begins to appear. After 30 min sputtering, both $Fe2p_{3/2}$ and $Fe2p_{1/2}$ peaks are clearly visible, confirming the existence of the magnetic material at this depth. The thickness of the shell can thus be estimated to be about 20–30 nm. Taking into account the magnetic core (ca. 20 nm), the particle size of ASA-LDHs/$MgFe_2O_4$-24 is estimated to be ca. 50 nm or above due to the obvious aggregating trend of magnetic material, in agreement with TEM results. Though the intensities of $Fe2p_{3/2}$ at 710.7 eV and Mg2*p* at 50 eV are relatively weak, the Zn/Fe ratio on the surface is estimated as 399, which is much greater than that in bulk ASA-LDHs/$MgFe_2O_4$-24 (Zn/Fe = 29) based upon ICP analysis. For this reason, the Mg and Fe are mostly situated in the interior rather than on the surface, revealing a core–shell structure involving $MgFe_2O_4$ embedded in the nucleus coated with ASA-LDHs phase.

In addition, from Table 2, the binding energy of Mg2*p* in ASA-LDHs/$MgFe_2O_4$-24 is remarkably larger than that in $MgFe_2O_4$. Chemical shifts arise from the variation of electrostatic screening experienced by core electrons, as valence electrons are drawn towards or away from the

Table 2
The XPS data of ASA-LDHs/$MgFe_2O_4$, ASA-LDHs and $MgFe_2O_4$

	Binding Energy (eV)					
	$Zn2p_{3/2}$	Al2*p*	O1*s*	C1*s*	Mg2*p*	$Fe2p_{3/2}$
ASA-LDHs/$MgFe_2O_4$	1021.9	74.5	535.2	284.6	50.0	710.7
ASA-LDHs	1021.8	74.3	532.6	284.6	—	—
$MgFe_2O_4$	—	—	—	—	48.8	710.9
For ASA-LDHs/$MgFe_2O_4$-24		Surface[a]			Bulk[b]	
Zn/Fe (mol/mol)		399			29	
Zn/Al (mol/mol)		3.6			3.3	

[a]Based upon XPS analysis.
[b]Based upon ICP analysis.

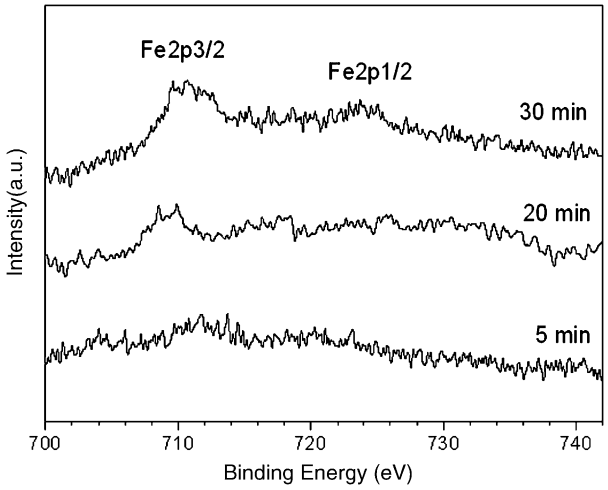

Fig. 7. The XPS spectra of Fe2*p* of different depth profiles below the surface layer of ASA-LDHs/$MgFe_2O_4$-24.

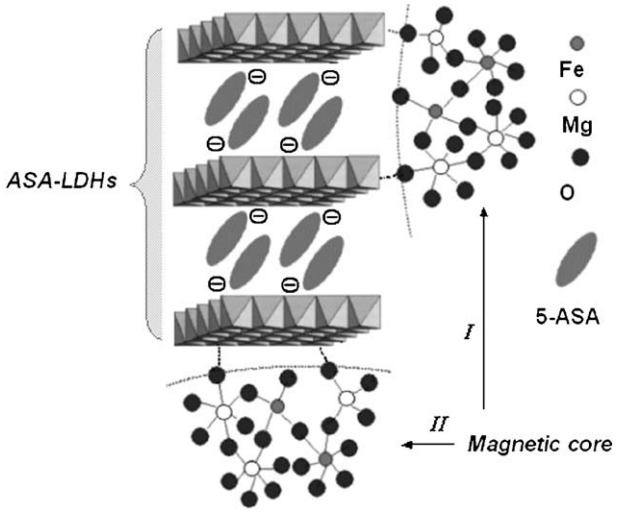

Fig. 8. Schematic structural model of magnetic 5-ASA intercalated LDHs composite.

atom [39]. The electronegativity of the element varies in the order Fe > Zn > Al > Mg. Consequently, the variation in chemical shifts of Mg2*p* could account for an interaction between the ASA-LDHs phase and the magnetic core $MgFe_2O_4$ probably through Zn–O–Mg and Al–O–Mg bonds formed at the interface. Thus, the electron density around Mg^{2+} nucleus decreases as Mg^{2+} is linked with Zn^{2+} or Al^{3+} through oxygen atoms, inducing a weak electrostatic shielding for Mg^{2+} nucleus, and resultantly the binding energy increases for Mg2*p*. Considering the deductions above, the introduction of $MgFe_2O_4$ should lead to the slightly larger binding energy of $Zn2p_{3/2}$ and Al2*p* for ASA-LDHs/$MgFe_2O_4$-24 than those for ASA-LDHs. Moreover, being consistent with the TG-DTA analyses, the improved thermal stability of ASA-LDHs/$MgFe_2O_4$-24 can be partially ascribed to the existence of Zn–O–Mg and Al–O–Mg linkages between the Zn–Al layer of ASA-LDHs and $MgFe_2O_4$.

Taken together, these results confirm not only an interaction between 5-ASA and $MgFe_2O_4$ but lead us to envisage the possibility of a real core–shell magnetic organic–inorganic hybrid composite formed by coprecipitation self-assembly technique. A schematic structural model of a magnetic nanosized organic–inorganic hybrid material involving ASA-LDHs and $MgFe_2O_4$ is tentatively proposed in Fig. 8. There are two possible connection approaches between ASA-LDHs layer and $MgFe_2O_4$ phase: (I) Zn–O–Mg and Al–O–Mg linkages parallel to the LDH layers; (II) Zn–O–Mg and Al–O–Mg linkages perpendicular to the LDH layers. The former is preferred because of the more unsaturated sites localized near the edge of LDH layer favoring the formation of Zn–O–Mg and Al–O–Mg linkages along this direction. The tilted close-packed bilayer orientation of 5-ASA in magnetic 5-ASA intercalated LDHs composites is previously described in Section 3.2.

4. Conclusions

A magnetic layered organic–inorganic hybrid material involving 5-ASA intercalated Zn–Al LDHs and magnesium ferrite ($MgFe_2O_4$, which was derived from Mg–Fe LDHs) is assembled by a coprecipitation self-assembly method. The crystal structure analyses illustrate that the ordered but relatively strong reflections of 5-ASA intercalated LDHs and the clear but weak diffractions of $MgFe_2O_4$ are coexisted in the magnetic composite. TEM image shows that the 5-ASA intercalated LDHs layer covers the $MgFe_2O_4$ particles. The particle size of magnetic 5-ASA intercalated LDHs is of 50–80 nm. The saturation magnetization of magnetic 5-ASA intercalated LDHs composites increases with increasing addition of $MgFe_2O_4$ magnetic core. The TG-DTA analyses indicate the improved thermal stability of 5-ASA in magnetic hybrids, implying their facilitating longer storage character for drug. The 5-ASA loading increases with decreasing Zn/Al ratio of magnetic 5-ASA intercalated LDHs composites. The XPS analyses demonstrate a majority of Zn, Al and O atoms on the surface of magnetic particles. It is believed that the magnetic core $MgFe_2O_4$ is coated with 5-ASA intercalated LDHs layer probably through Zn–O–Mg and Al–O–Mg linkages, and consequently a core–shell structural model is revealed and schematically presented. Introducing magnetic properties into nanosized organic–inorganic drug intercalated LDHs composite by introducing magnetic cores may offer broad perspectives in drug targeting system.

Acknowledgment

Authors thank financial support from National Natural Science Foundation of China (Grant no. 90306012).

References

[1] R. Allmann, Chimia 24 (1970) 99.
[2] F. Cavani, F. Trifiro, A. Vaccari, Catal. Today. 11 (1991) 173.
[3] A. Goodman-Gilman, L.S. Goodman, A. Gilman, The Pharmacological Basis of Therapeutics, MacMillan Publishing Co, Inc., New York, 1996, p. 995.
[4] F. Trifiro, A. Vaccari, in: J.L. Atwood, J.E.D. Davies, D.D. MacNicol, F. Vogtle, J.M. Lehn, G. Alberti, T. Bein (Eds.), Comprehensive Supramolecular Chemistry, vol. 7, Pergamon Press, Oxford, 1996, p. 251 (Chapter 10).
[5] A.I. Khan, D. O'Hare, J. Mater. Chem. 12 (2002) 3191.
[6] A.I. Khan, L.X. Lei, A.J. Norquist, D. O'Hare, Chem. Commun. (2001) 2342.
[7] V. Ambrogi, G. Fardella, G. Grandolini, L. Perioli, M.C. Tiralti, AAPS PharmSciTech. 3(3) (2002) article 26.
[8] V. Ambrogi, G. Fardella, G. Grandolini, L. Perioli, Int. J. Pharm. 220 (2001) 23.
[9] W. Selby, Vet. Microbiol. 77 (2000) 505.
[10] M. Saffran, G.S. Kumar, C. Savariar, J.C. Burnham, F. Williams, D.C. Neckers, Science 233 (1986) 1081.
[11] S.S. Davis, J.G. Hardy, J.W. Fara, Gut 27 (1986) 886.
[12] A.A. Salayers, J.A.Z. Leedle, in: D.J. Hentges (Ed.), Human Intestinal Microflora in Health and Disease, Academic Press, London, United Kingdom, 1983, p. 129.
[13] D. Pouliquen, C. Chouly, Magnetic microcarriers for medial applications, in: R. Arshady (Ed.), Microspheres Microcapsules & Liposomes, Medical and Biotechnology Applications, vol. 2, Citus Books, London, 1999, pp. 343–382.
[14] A. Senyei, K. Widder, G. Czerlinski, J. Appl. Phys. 49 (6) (1978) 3578.
[15] M.A. Rettenmaier, J.A. Stratton, P.J. Disaia, M.L. Berman, A. Senyei, K.J. Widder, Gynecol. Oncol. 20 (2) (1985) 268.
[16] J.L. Arias, V. Gallardo, S.A. Gomez-Lopera, R.C. Plaza, A.V. Delgado, J. Controlled Release. 77 (2001) 309.
[17] K.J. Widder, R.M. Morris, G.A. Poore, D.P. Howard, A.E. Senyei, Eur. J. Cancer Clin Oncol. 19 (1983) 135.
[18] J.Y. Sun, H.Y. Du, Inorganic Material Manufacture and Application, Chemical Industry Press, Beijing, 2002.
[19] A. Kondo, H. Fukuda, J. Ferment. Bioeng. 84 (1997) 337.
[20] A. Masanori, H. Hiroshi, N. Kazuhiro, Jpn. Kokai Tokkyo Koho JP 2002131320 A2 9.
[21] J.S. Kawaguchi, K. Misawa, Jpn. Kokai Tokkyo Koho JP 2002139496 A2 17.
[22] V. Šepelák, D. Schultze, F. Krumeich, U. Steinike, K.D. Becker, Solid State Ionics 141-142 (2001) 677.
[23] S.A. Oliver, R.J. Willey, H.H. Hamdeh, G. Oliveri, G. Busca, Scripta Metall. Mater. 33 (1995) 1695.
[24] Q. Chen, A.J. Rondinone, B.C. Chakoumakos, Z.J. Zhang, J. Magn. Magn. Mater. 194 (1999) 1.
[25] J.J. Liu, F. Li, D.G. Evans, X. Duan, Chem. Commun. 2 (2003) 542.
[26] H. Zhang, Q. Qi, D.G. Evans, X. Duan, J. Solid State Chem. 177 (2004) 772.
[27] X. Duan, Q.Z. Jiao, L. Li, Chinese Patent CN 99119385.7.
[28] X. Duan, Q.Z. Jiao, Chinese Patent CN 00132145.5.
[29] Y. Zhao, F. Li, R. Zhang, D.G. Evans, X. Duan, Chem. Mater. 14 (2002) 4286.
[30] S.J. Blundell, Magnetism in Condensed Matter, Oxford University Press, New York, 2001, pp. 131–136.
[31] S.P. Newman, W. Jones, New J. Chem. (1998) 105.
[32] F. Kooli, I.C. Chisem, M. Vucelic, W. Jones, Chem. Mater. 8 (1996) 1969.
[33] Sadtler Standard Spectra: IR 33100K.
[34] N. Zerrouk, J.M.G. Dorado, P. Arnaud, C. Chemtob, Physical characteristics of inclusion compounds of 5-ASA in α and β cyclodextrins, Int. J. Pharm. 171 (1998) 19.
[35] M.Z.B. Hussein, Z. Zainal, A.H. Yahaya, D.W.V. Foo, J. Controlled Release 82 (2002) 417.
[36] M.J. O'Neil, M.J. O'Neil, in: The Merck Index, 13th ed, Merck & Co., Whitehouse Station, NJ, 2001.
[37] A.I. Tsyganok, K. Suzuki, S. Hamakawa, K. Takehira, T. Hayakawa, Catal. Today 77 (2001) 75.
[38] D. Briggs, M.P. Seah, in: Practical Surface Analysis by Auger and X-ray Photoelectron Spectroscopy, Wiley, New York, 1983.
[39] J.M. Walls, in: Methods of Surface Analysis, Cambridge University Press, Cambridge, 1989.